Unraveling the structural dependency of Weyl nodes in Co_2MnGa

N. Schulz,[1] G. Pantano,[1] D. DeTellem,[1] A. Chanda,[1] E. M. Clements,[2] M. McGuire,[2] A. Markou,[3] C. Felser,[4] D. A. Arena,[1] J. Gayles,[1,*] M. H. Phan,[1] and H. Srikanth[1,†]

[1]*Department of Physics, University of South Florida, Tampa, Florida 33620, USA*
[2]*Oak Ridge National Laboratory, Oak Ridge, Tennessee 37831, USA*
[3]*Physics Department, University of Ioannina, 45110 Ioannina, Greece*
[4]*Max Planck Institute for Chemical Physics of Solids, 01187 Dresden, Germany*

(Received 8 June 2024; accepted 15 July 2024; published 9 August 2024)

Conventionally, the modulation of the intrinsic Weyl nodes in Weyl semimetals is challenging, due to topological protection. Here we report the structural dependence of the Weyl nodes in a Co_2MnGa Heusler thin film via a temperature-dependent tetragonal distortion. The ability to manipulate these Weyl nodes allows for the control of the intrinsic electromagnetic properties. Temperature-dependent x-ray diffraction (XRD) measurements identify a compressive tetragonal distortion with decreasing temperature from 300 to 20 K. The calculated Weyl properties can be directly compared with experimental parameters through the temperature-dependent XRD measurements which show the intrinsic correlation between Weyl properties and important magnetic parameters. The microscopic momentum space properties of Weyl nodes such as the distance (d_W), solid angle (Ω_W), tilt (φ_W), and nodal point energy (E_W) directly affect the macroscopic observable properties such as exchange stiffness (A), magnetization (M), and effective anisotropy field (H_K^{eff}), as shown via structure-dependent density functional theory calculations. These predictions are experimentally observed as large variations in the bulk magnetization and effective anisotropy field as a function of temperature. These results highlight a unique degree of freedom in the control of macroscopic magnetic properties via the modulation of the intrinsic properties of Weyl nodes through structural distortions.

DOI: 10.1103/PhysRevB.110.054419

I. INTRODUCTION

The existence of Weyl fermions as quasiparticle excitations in solid state systems is directly tied to the crystal and magnetic space group symmetry which requires the lack of either time reversal or inversion symmetry [1]. The number and positions of the Weyl nodes in these systems therefore depends on the conserved crystal symmetries during adiabatic processes like structural changes as well as the magnetization direction [2]. The impacts of these conserved symmetries have been studied in Weyl semimetal systems theoretically by tuning the n-fold rotational symmetry [3], stabilizing double Weyl phonons [4], and examining maximally charged Weyl points [5].

Within Weyl semimetal systems, the preserved crystal symmetries play an important role in the determination of the bulk electronic and magnetic properties. Changing temperature or applied external fields can be utilized for the reduction of these symmetries [6]. Potential Weyl semimetal systems that exhibit temperature-dependent crystal structure changes are then of particular interest to study the interplay of these symmetries, Weyl points, and magnetic properties. Manipulating Weyl points through symmetry modulation provides an additional degree of freedom to exploit in the design of topologically nontrivial materials.

Heusler compounds have proven to be a broad platform for the study of a wide range of emergent phenomena such as Weyl and Dirac fermions [7–11], compensated magnets [12–14], spin-gapless semiconductors [15–17], half-metals [18–20], and magnetic shape memory [21–23]. One can tune the chemical composition, and site occupation which allows for the selection of these emergent phenomena, giving this class of materials a wide range of applicability [24]. Yet stoichiometric variations can be impractical for device applications and can lead to drastic changes in the electronic structure. An alternative means of manipulating the magnetic and electronic properties in Heusler compounds is through structural changes, of which cubic $L2_1$ structures exhibit magnetic and electronic properties that are highly sensitive to tetragonal distortions [25,26]. These distortions have been studied in the context of their impact on magnetic shape memory [22,27–29], magnetic anisotropy [30,31], and spin transfer torques [32–34], which depend on the respective c/a ratio of the tetragonal distortion.

Here, we report on the temperature-dependent tetragonal distortion in a ferromagnetic Heusler Weyl semimetal, Co_2MnGa. The ambient single crystal structure of Co_2MnGa belongs to the $Fm\bar{3}m$ space group (No. 225) with the corresponding point group O_h^5 [35]. Co_2MnGa has been shown theoretically to exhibit three interconnected nodal lines without spin-orbit coupling that form in the k_x, k_y, and k_z

*Contact author: gayles@usf.edu
†Contact author: sharihar@usf.edu

directions, protected by the mirror symmetries M_x, M_y, and M_z and related by C_4 rotational symmetries [8,9,35,36]. However, taking spin-orbit coupling into account and the spontaneous magnetization direction to be along the [110] direction, the nodal lines gap and the Weyl nodes emerge due to combined inversion and rotational symmetries [7,8,35,37]. Specifically, a group of eight symmetry elements, defined by the three generators: inversion ($\hat{\boldsymbol{\imath}}$), twofold rotation around the [1–10] axis with time reversal ($\hat{T}C_2$[1-10], and twofold rotation around the [001] axis (C_{2z})) allows for two pairs of Weyl points to form in the k_xk_y plane close to the Fermi energy [7,8]. The Weyl points are protected by different eigenvalues of the time reversal $\hat{T}C_2$[1-10] symmetry operation, formed by two crossing majority spin bands, and the pairs are related by inversion symmetry [7,8].

Our temperature-dependent x-ray diffraction (XRD) measurements show a contraction of the *c*/*a* lattice ratio as a function of decreasing temperature. The tetragonal distortion reduces the crystal symmetries to the *I*4/*mmm* space group (No. 139) with the corresponding D_{4h}^{17} point group. Consequently, the Weyl points shift off the high-symmetry k_xk_y plane reducing the number of preserved symmetries to 4 with the two generators: $\hat{\imath}$ and $\hat{T}C_2$ [1–10]. Structure-dependent density functional theory (DFT) calculations indicate that intrinsic parameters of the Weyl nodes, such as the Weyl distance in momentum space (d_{W}), Weyl solid angle (Ω_{W}), Weyl tilt (φ_{W}), and nodal point energy (E_{W}), directly affect macroscopic parameters such as the exchange stiffness (A) as a function of tetragonal distortion. It is seen that under specific ranges of *c*/*a* ratios, there exist strong nonlinear changes in these intrinsic properties, which can be directly compared to measured changes in the bulk and surface magnetic properties. Temperature-dependent magnetic measurements display pronounced nonmonotonic changes in the saturation magnetization (M_{S}) and differences between the field cooled cooling (FCC) and field cooled warming (FCW) measurement protocols. The changes occur at the same *c*/*a* ratios that are predicted via DFT calculations, congruently mapped through XRD measurements. Tunnel diode oscillator-based transverse susceptibility measurements, which probe the effective anisotropy field of the system as a function of temperature, further connect the macroscopic magnetic properties to changes in the intrinsic properties of the Weyl points.

Finally, to independently probe the surface magnetic properties, temperature-dependent magnetic force microscopy measurements were performed. All magnetic measurements show strong nonlinear changes in the magnetic properties arising due to the weak temperature-dependent tetragonal distortion of the $L2_1$ cubic structure as a function of temperature, and its symmetry-dependent modulation of the Weyl points. Our results indicate that small changes in the *c*/*a* ratio can give rise to comparatively large changes in the bulk magnetic properties due to predicted modulations of the intrinsic electronic properties of the Weyl points [6].

II. RESULTS AND DISCUSSION

Figures 1(a) and 1(b) show the temperature (T) dependent (002) and (004) x-ray diffraction (XRD) reflections of the 80 nm thick Co_2MnGa film within the temperature range of 300–20 K. The growth procedure and in-depth characterization of these films have been reported elsewhere [25]. Since the films are epitaxially grown, only *c* axis reflections are visible in $\theta-2\theta$ scans. The (002) and (004) reflections shift monotonically to higher 2θ on cooling, and are expressed as a change in the *c* lattice parameter with respect to the room temperature *a* value [Fig. 1(c)], where the shaded regions are highlighted for connection between theory and experiment. The temperature dependence of the *c*/*a* ratio is well described by the Debye model of thermal expansion, which for low temperatures predicts that $c \propto T^3$, and for intermediate higher temperatures below the Dulong-Petit limit, $c \propto T$ [38]. Figure S1 shows the normalized temperature dependence of *c* for both the MgO (substrate) and Co_2MnGa. Although both the MgO substrate and Co_2MnGa film follow similar temperature dependencies as described by the Debye model, their respective rates of change of their lattice constants differ, with Co_2MnGa changing much more rapidly over the same temperature range, giving rise to strain at the interface (see the Supplemental Material [39]). Figure S2 shows the reciprocal space mapping of the in-plane (220) reflection at room temperature. The reciprocal space map shows that there exists uniform elongation along both q_x and q_y corresponding to the reciprocal space representation of the spatial coordinates x and y, a sign of homogeneous in-plane strain [40]. Figure 1(d) shows a schematic of the change in crystal symmetry when going from a cubic to tetragonally distorted structure, and its impact on the Weyl solid angle (Ω_{W}), Weyl distance (d_{W}), Weyl tilt (φ_{W}), and nodal point energy (E_{W}). Here Ω_{W} is defined as the solid angle made by the cone generated by the Weyl points in steradians, d_{W} is the distance between respective Weyl points in reciprocal space, and φ_{W} is the tilt angle formed with respect to a perpendicular cone generated by the undistorted Weyl point. Figure 1(e) shows the bulk Brillouin zone with respective points of high-symmetry and Weyl points labeled. Shown are comparisons of the cubic ($c/a = 1$) and most distorted ($c/a = 0.990$) cases. For nonzero distortions, the Weyl nodes shift off the high-symmetry paths obtaining a finite z component leading to the changes observed in the inset of Fig. 2(a).

DFT calculations were performed to examine the change in these parameters as a function of the *c*/*a* ratio. Figure 2(a) shows the calculated band structures for *c*/*a* ratios of 1 (black) and 0.990 (red). The full list of band structures for the utilized *c*/*a* values can be seen in Fig. S3 [39]. There exist clear changes in the electronic properties even under small tetragonal distortions. This is further highlighted in the inset of Fig. 2(a), which shows the energy momentum dispersion zoomed in around a Weyl point. Figure 2(b) shows the d_{W} as a function of *c*/*a*. These distances are defined as the distance between respective Weyl points in reciprocal space, where d_1, d_2, and d_3 correspond to the distances between n_1 and n_2, n_3, and n_4, respectively. A schematic representation of a cross section of these distances can be seen in Fig. S4 [41]. There exist three distinct regions in which the Weyl distances change corresponding to $0.993 \leqslant \frac{c}{a} \leqslant 1$, $0.992 \leqslant \frac{c}{a} < 0.993$, and $0.990 \leqslant \frac{c}{a} < 0.992$. In particular the distances exhibit a local maxima around these regions. These *c*/*a* values can be mapped to the temperature ranges of $T > 275$ K, $200\ \mathrm{K} \leqslant T \leqslant 275$, and $T < 200$ K in our film. Figure 2(c) shows the Ω_{W} and

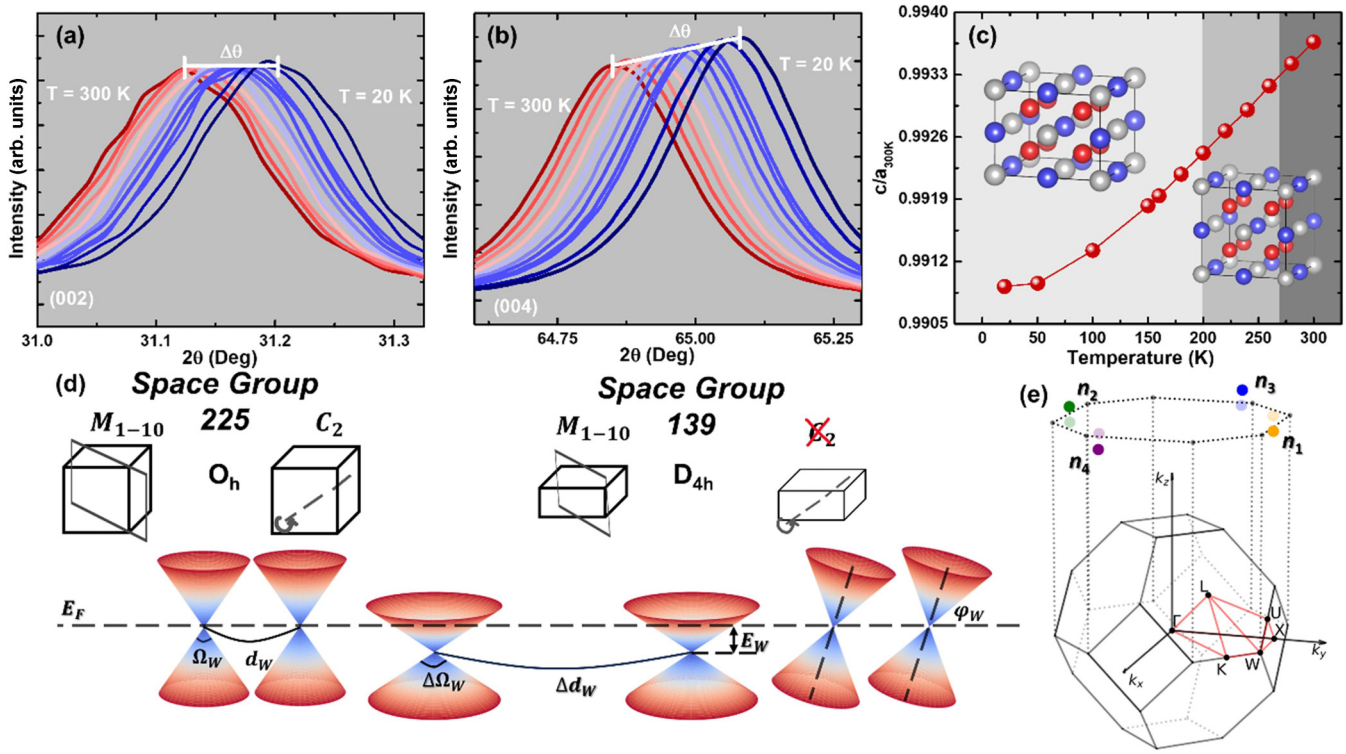

FIG. 1. (a,b) Temperature dependence of the (002) and (004) reflections, respectively ($\Delta\theta$ highlights the total change in 2θ across the temperature range). (c) Temperature dependence of the c/a lattice constant ratio. (d) Schematic representation of the changes in structural symmetry going from cubic to tetragonal, and its impact on the band structure. (e) Bulk Brillouin zone (BZ) for Co_2MnGa with the high-symmetry and Weyl points labeled. The (001) BZ plane is projected to show the position of the Weyl crossings for both the $c/a = 1.000$ (light) and $c/a = 0.990$ (dark) cases.

φ_W, as a function of c/a, while Fig. 2(d) shows the energy shift of the Weyl points with respect to the Fermi energy (E_W) and exchange stiffness (A) as a function of c/a. The same c/a regions have been highlighted for clarity. In Fig. 2(c) the respective Weyl solid angle and tilt angles change across the same c/a ranges as specified previously, with large changes occurring (~60% larger than room temperature c/a) in Ω_W across $c/a = 0.990$. The energy shift shown in Fig. 2(d) follows an opposite pattern to the Weyl distances, suggesting that shorter Weyl distances (closer together in momentum space) correspond to smaller energy shifts with respect to the Fermi energy.

To explore the impacts of the predicted changes in the magnetic and electronic properties as a function of the tetragonal distortion, magnetization (M) versus temperature (T) and magnetic field (H) measurements were performed with the field applied in plane with respect to the sample surface. Figure 3(a) shows the M-H loops recorded at $T = 40$ and 300 K, respectively. The films show an in-plane easy axis, and a saturation magnetization $M_S \approx 910 \frac{\text{emu}}{\text{cm}^3}$ at 300 K, in agreement with previous results [25,42]. Figure 3(b) shows the temperature-dependent magnetization [$M(T)$] following the field cooled cooling (FCC) and field cooled warming (FCW) protocols under different applied fields, measured from $H =$ 25 to 5000 Oe (selected fields shown for clarity). Two distinct changes in the magnetic properties of these films are seen, first a shallow peak at $T_1 \sim 270$ K [as taken from the low field $M(T)$ measurement], which also marks the onset of thermal hysteresis, followed by an inflection point at $T_2 \sim 200$ K. It should be noted that Co_2MnGa has an ordering temperature of $T_c = 694$ K, far above the temperature range in question [25]. Therefore, these features are not related to an ordering temperature. The observed behavior of the magnetization and thermal hysteresis are similar to the martensitic transformations which have been reported in other Heusler alloys, which arises due to a temperature-dependent tetragonal distortion of the crystal structure [28,29,41,43] from a high-temperature cubic structure to a lower-symmetry structure at low temperatures. In this case the martensiticlike behavior may be driven by the interplay between the temperature-dependent strain due to both the substrate/film lattice mismatch, as well as due to differing coefficients of thermal expansion, which leads to the tetragonal distortion of the cubic crystal structure. This is further evidenced by the kinetic arrest phenomena [42,44] observed at an applied field of $H = 50\,000$ Oe, shown in Supplemental Fig. S5 [39], where the transformation is weakened under large applied fields. Furthermore, T_1 shows a strong field dependence, as shown in Fig. 3(c), whereas T_2 effectively shows no field dependence [39]. Care should be taken when examining the shaded regions which highlight the onset of T_1 because, since it is field dependent, the temperatures at which T_1 occurs are different depending on whether the measurement is taken in a saturated state or a demagnetized state. When the saturation magnetization (M_S) is extracted from the M-H measurements, as shown in Fig. 3(d), a similar trend is observed. Namely, there exists a local maximum at T_1, and

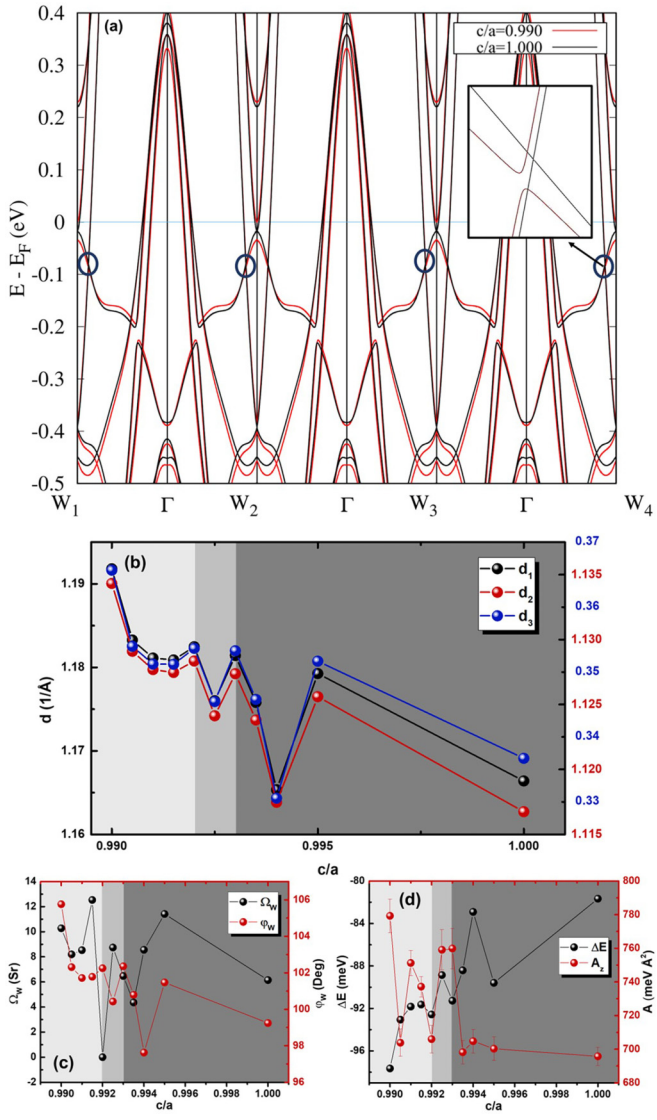

FIG. 2. (a) Sample energy momentum dispersions for $c/a = 0.990$ (red) and 1 (black). (b) Weyl distances as a function of c/a. (c) Weyl solid angle and tilt angle extracted from the band structures as a function of c/a. (d) Exchange stiffness and nodal point energy as a function of c/a.

then an inflection point at T_2, below which a steep decrease in the saturation magnetization as compared to the room temperature value occurs. These temperatures are mapped to their respective c/a ratios through the temperature-dependent XRD data shown in Fig. 1(c). From these data, T_1 corresponds to a c/a ratio of approximately 0.993, while T_2 corresponds to a c/a ratio of 0.992. These values have been highlighted in Figs. 2(b)–2(d), which are the exact values marking large changes in the nodal point energy, exchange stiffness, Weyl solid angle, and Weyl distances. In the context of Figs. 3(b) and 3(d) compared with Figs. 2(b)–2(d), higher magnetization values correspond to Weyl points that are further apart and shifted away from the Fermi energy.

TDO (tunnel diode oscillator) based transverse susceptibility (TS) measurements were then performed to probe the changes in the effective anisotropy of the system as a function of temperature [45–49]. Since Co_2MnGa exhibits strong in-plane anisotropy, the TS measurements are performed by sweeping a static out of plane magnetic field with respect to the sample surface, and a fixed in-plane oscillating rf field of $H \sim 10$ Oe. Figure 4(a) demonstrates bipolar TS spectra at $T = 300$ K. High-field peaks in the TS spectra are fit with a peak finding function to determine the peak position, which corresponds to the effective anisotropy field (H_K^{eff}) of the system at a given temperature. Low-field peaks correspond to the switching field (H_{sw}) [50]. This procedure is repeated for all the temperatures in question. Figure 4(c) shows the temperature dependence of H_K^{eff}. Again, pronounced changes in H_K^{eff} are observed at the same temperature/(c/a) ranges reported earlier, matched to their respective closest temperatures. Additionally, the domain wall width, and thus the domain width in magnetic systems, is highly sensitive to both the exchange stiffness and the anisotropy energy density as [51]

$$\delta_{\text{DW}} = \pi \sqrt{\frac{A(T)}{K(T)}}.$$

To connect the simulated changes in the exchange stiffness to the measured H_K^{eff}, temperature-dependent magnetic force microscopy (MFM) measurements were performed. A magnetic domain structure imaged at a representative temperature (275 K) is shown in Fig. 4(b), which shows wavelike domain structure (additional temperatures and scales shown in Fig. S7 [39]), which further shows textured domains along the direction of the MgO substrate, indicative of the impact of strain even on the surface magnetic domains [39]. By a comparison of Fig. 4(b) and Fig. S7 [39] it can be seen that the magnetic domains expand and contract following the changes in the bulk magnetic properties induced by the temperature-dependent tetragonal distortion. At temperatures from each MFM scan the autocorrelation spectra and phase distribution can be extracted, as shown in Figs. S8(a) and S8(b), respectively [39]. By fitting both the two-dimensional (2D) autocorrelation and phase distribution with Gaussians as a function of temperature, the average domain width and root-mean-squared phase deviation ($\Delta\varphi_{\text{rms}}$) can be extracted as a function of temperature [52,53], shown in Fig. 4(d); larger range scans were performed to obtain the statistics over a larger number of domains while smaller scale scans are shown in Fig. S7 [39]. The phase distribution and average domain width follow opposite patterns through $T \approx 200$ K, then converge at lower temperatures. As has been reported previously, $\Delta\varphi_{\text{rms}}$ follows the temperature-dependent surface magnetization of the sample, which agrees well with the magnetization data as well as the structure dependence of A extracted from DFT calculations, occurring at temperatures for T_1 which correspond to a demagnetized state. The temperature dependence of H_K^{eff} and the average domain width follow the same trend. This highlights the reproducible impact of the structural modulations of d_W and A on both the average domain width and anisotropy field. Moreover, Fig. S9 clearly indicates the occurrence of in-plane negative magnetoresistance in the Co_2MnGa film across the temperature range in question [39]. This negative magnetoresistance has been reported extensively as a feature of Weyl semimetals and

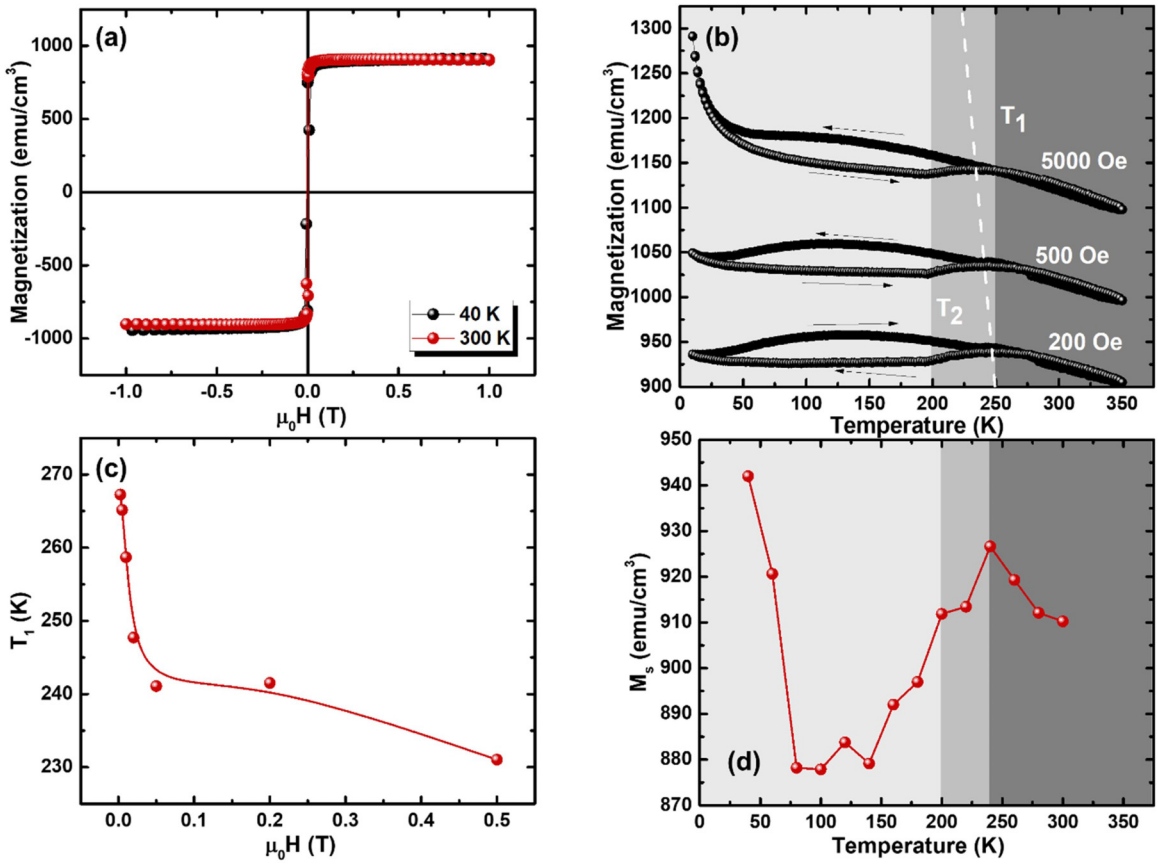

FIG. 3. (a) Sample field-dependent magnetization measurements at 300 and 40 K. (b) Magnetization versus temperature measurements following field cooled cooling/field cooled warming protocols under different static applied fields. (c) Field dependence of T_1, marking the onset of thermal hysteresis. Lines are to guide the eyes. (d) Temperature dependence of the saturation magnetization as extracted from the high-field magnetization measurements.

is therefore suggestive of the preservation of the Weyl points in Co_2MnGa films even under the large changes in magnetic and electronic properties due to the temperature-dependent tetragonal distortion [54–56].

Furthermore, calculations of the net magnetic moment and the magnetocrystalline anisotropy as a function of *c*/*a* indicate linear changes of the moment, and negligible ($\sim \mu$eV) changes in the magnetocrystalline anisotropy. This underscores the dominant impact of the modulation of the microscopic Weyl distances, energy, and angles on the relevant macroscopic parameters including the exchange stiffness, saturation magnetization, and effective anisotropy, and their dependence on both temperature and applied magnetic field.

III. CONCLUSION

The impact of a tetragonal distortion on the surface and bulk magnetic properties was studied in the magnetic Weyl semimetal Co_2MnGa. It was found that the temperature-dependent tetragonal distortion leads to changes in the intrinsic properties of Weyl nodes including the Weyl solid angle, distances, tilt, the nodal point energy which gives rise to comparatively larger impacts in the macroscopic properties including the exchange stiffness, saturation magnetization, and effective anisotropy field. These changes in the properties of the Weyl points are found to be intrinsically related to the bulk magnetic properties, amplified even under small tetragonal distortions. This gives rise to nonmonotonic changes in the bulk and surface magnetic properties as a function of temperature manifested through a weak martensiticlike transition, while preserving Weyl points against these structural changes. Temperature-dependent structural distortions can therefore be utilized as an alternative degree of freedom in the manipulation of the bulk magnetic and electronic properties in Weyl semimetal systems.

IV. METHODS

Thin film growth and characterization. An 80 nm thick (001)-oriented Co_2MnGa film was grown on a (001)-oriented MgO single-crystal substrate using a BESTEC ultrahigh-vacuum magnetron sputtering system. Prior to deposition, the chamber was evacuated to a base pressure of less than 6×10^{-9} mbar, while the process gas (Ar 5N) pressure was maintained at 3×10^{-3} mbar. The target to substrate distance was set to 20 cm, and the substrate was rotated at 20 rpm to ensure uniform growth. We used Co (5.08 cm), Mn (5.08 cm), and $Mn_{50}Ga_{50}$ Si (5.08 cm) sources in a confocal geometry, applying 34, 6, and 20 W dc power, respectively. The films were grown at 600 °C, followed by an additional 30 min of *in situ* postannealing at the same temperature. A protective

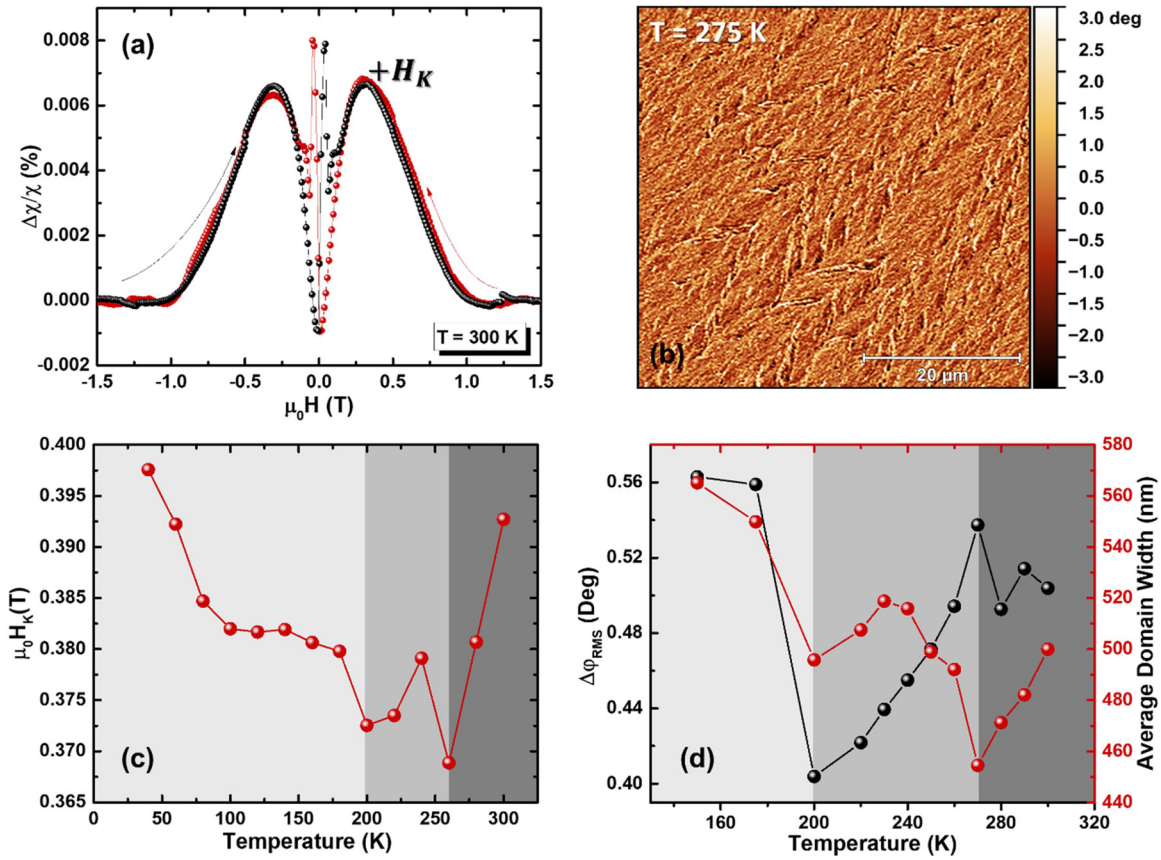

FIG. 4. (a) Transverse susceptibility spectra taken at 300 K. (b) Magnetic force microscopy scan at 275 K. (c) Effective anisotropy field as a function of temperature, extracted from transverse susceptibility measurements. (d) The rms phase deviation and average domain width as a function of temperature.

layer of amorphous 3 nm thick Si film was deposited at room temperature, to prevent oxidation of the film.

Temperature-dependent x-ray diffraction. Temperature-dependent x-ray diffraction measurements were conducted with a PANalytical X'Pert Pro powder diffractometer using monochromated Cu $K\alpha$ radiation. The temperature was controlled with an Oxford Phenix closed cycle cryostat. Diffraction scans were collected using a $\theta-2\theta$ protocol with the x rays normal to the film surface oriented vertically. It should be noted that since the films are epitaxially grown, $\theta-2\theta$ scans show only c-axis reflections as expected. The value for a was assumed to be fixed at the MgO c value corrected for the misfit strain as was reported previously [25]. Room temperature in-plane reciprocal space mapping was performed using a Rigaku SmartLab diffractometer. Scans were performed using a planar beam configuration and Cu $K\alpha$ radiation.

Theory and computation. The electronic structure and exchange stiffness calculations were performed using the full potential linearized augmented plane wave (FLAPW) method with FLEUR [57]. The calculations were carried out within the Perdew-Burke-Ernzerhof exchange-correlation functional [58]. Convergence was reached for a plane-wave cutoff of 3.8 a.u.$^{-1}$ (inverse atomic units) and a k-point grid of 18^3. The cubic unit cell of the bulk Heusler compound Co_2MnGa consists of four interpenetrating FCC sublattices with the experimental lattice constant of 5.77 Å. The Co, Mn, and Ga atoms occupy the Wyckoff positions 8c ($\frac{1}{4}$, $\frac{1}{4}$, $\frac{1}{4}$) and ($\frac{3}{4}$, $\frac{3}{4}$, $\frac{3}{4}$), 4b ($\frac{1}{2}$, $\frac{1}{2}$, $\frac{1}{2}$), and 4a (0,0,0), respectively [40].

We performed self-consistent total energy calculations of magnetic spin spirals to obtain the exchange stiffness. The exchange stiffness was extracted for each c/a ratio by performing a least-squares fit for the total energy of the system as a function of the spin spiral wave vector $\vec{q} = q\hat{z}$ using the equation $E(q) = Aq^2$ where A is the exchange stiffness [35]. The fitting is shown in Fig. S6 in the Supplemental Material [39].

We confirmed the point group and magnetic group symmetries with the ISOTROPY software and with the Bilbao Crystallographic Server [59,60]. Figure 2(a) shows the four relevant linear crossings. A dense k-point grid of ($25 \times 25 \times 25$) was used to examine the energy dispersion close to the Weyl points of interest with a uniform spacing of 10^{-7} between each point. We determined, due to the shifting of the Weyl points off the high-symmetry k_xk_y plane in the Brillouin zone, that the symmetry operations along the magnetization direction [001] and the [110] direction were lost. The shifting of the Weyl points within the Brillouin zone is illustrated in Fig. 2(a). A gap appears where the Weyl point has shifted away from the high-symmetry path as compared to the cubic case.

The nodal point energy (E_W) is the difference in energy between the Fermi level and the average energy of the two

intersecting bands at the minimum point (i.e., Weyl point). The distance of the Weyl points is calculated in the conventional reciprocal cell. The tilt (φ) and solid angles (Ω) were found by analyzing the shape of the energy surface near the Weyl point. The solid angle is calculated as $\Omega = 2\pi[1-\cos(\theta)]$ assuming a radius (i.e., the slanted height of the cone) to be 1 within a unit sphere.

Temperature-dependent magnetic force microscopy. Temperature-dependent MFM measurements were performed on a Hitatchi 5300E environmental control system under high-vacuum conditions ($P \leqslant 10^{-6}$ Torr). Prior to measurements, the MFM tip was magnetized out of plane using a permanent magnet. After the scans were completed, a parabolic background was subtracted to correct for flatness of the sample on the stage. Scanning line artifacts were then subtracted before applying a small Gaussian averaging/sharpening filter across the sample. The phase standard deviation was estimated by fitting a Gaussian distribution to the phase distribution at each temperature. Likewise, the average domain width was taken from the full width at half maximum (FWHM) of the 2D autocorrelation spectra at each temperature, with larger FWHM corresponding to larger domain widths. This was done by calculating the autocorrelation spectra at each temperature (see Fig. S8 [39]) and fitting different cross sections of the spectra with a Gaussian function to extract the FWHM, and therefore the average domain width across the image.

Magnetic characterization. Magnetometry measurements were performed utilizing the vibrating sample magnetometer (VSM) option of the Quantum Design Physical Properties Measurement System (PPMS). Samples were attached to a magnetically inert quartz rod via GE varnish. The magnetization as a function of field measurements reported had a standard linear diamagnetic background subtracted after each measurement. Measurements of magnetization as a function of temperature were performed in a zero field cooling (ZFC), field cooled cooling (FCC), field cooled warming (FCW) protocol where the samples were cooled to the measurement base temperature (10 K); then measurements were performed with the specified static applied magnetic field as the temperature was swept for each measurement.

Radio-frequency transverse susceptibility. Transverse susceptibility measurements were performed in a homemade setup inside of a PPMS. An *RLC* circuit is paired with a tunnel diode oscillator such that it is self-resonant at a resonance frequency of $f_{\text{res}} \approx 13$ MHz. The inductor of the circuit generates a fixed oscillating field of approximately 10 Oe. With the sample placed inside the inductor with the applied field out of plane with respect to the sample surface, the magnetic field of the PPMS is swept from $+H_{\text{sat}}$ to $-H_{\text{sat}}$ and back. Peaks in the transverse susceptibility spectra correspond to the effective anisotropy field of the system at a given temperature. These peaks are fit, and the peak location is determined from the fit parameters.

ACKNOWLEDGMENTS

H.S. and M.H.P. acknowledge support from the U.S. Department of Energy, Office of Basic Energy Sciences, Division of Materials Science and Engineering under Award No. DE-FG02-07ER46438. N.S. would like to acknowledge the Department of Defense SMART program. The work of E.M.C. and M.M. was supported by the U.S. Department of Energy (DOE), Office of Science, Basic Energy Services (BES), Materials Sciences and Engineering Division. The work of J.G. and G.P. was supported by the Air Force Office of Scientific Research under Award No. FA9550-23-1-0132. J.G. and G.P. acknowledge support from the Max Planck Society through the Max Planck Partner Group Programme.

[1] A. A. Zyuzin, S. Wu, and A. A. Burkov, Weyl semimetal with broken time reversal and inversion symmetries, Phys. Rev. B **85**, 165110 (2012).

[2] Z. Gao, M. Hua, H. Zhang, and X. Zhang, Classification of stable Dirac and Weyl semimetals with reflection and rotational symmetry, Phys. Rev. B **93**, 205109 (2016).

[3] C. Fang, M. J. Gilbert, X. Dai, and B. A. Bernevig, Multi-Weyl topological semimetals stabilized by point group symmetry, Phys. Rev. Lett. **108**, 266802 (2012).

[4] Y. J. Jin, Z. J. Chen, X. L. Xiao, and H. Xu, Tunable double Weyl phonons driven by chiral point group symmetry, Phys. Rev. B **103**, 104101 (2021).

[5] Q. Chen *et al.*, Discovery of a maximally charged Weyl point, Nat. Commun. **13**, 7359 (2022).

[6] Y. Tserkovnyak, Magnetic dynamics with Weyl fermions, Phys. Rev. B **103**, 064409 (2021).

[7] J. Kübler and C. Felser, Weyl points in the ferromagnetic Heusler compound Co_2MnAl, EPL **114**, 47005 (2016).

[8] Z. Wang, M. G. Vergniory, S. Kushwaha, M. Hirschberger, E. V. Chulkov, A. Ernst, N. P. Ong, R. J. Cava, and B. A. Bernevig, Time-reversal-breaking Weyl fermions in magnetic Heusler alloys, Phys. Rev. Lett. **117**, 236401 (2016).

[9] I. Belopolski *et al.*, Discovery of topological Weyl fermion lines and drumhead surface states in a room temperature magnet, Science **365**, 1278 (2019).

[10] M. M. Hosen *et al.*, Observation of Dirac state in half-Heusler material YPtBi, Sci. Rep. **10**, 12343 (2020).

[11] W. Meng, X. Zhang, Y. Liu, X. Dai, and G. Liu, Lorentz-violating Type-II Dirac fermions in full-Heusler compounds $X Mg_2Ag$ (X = Pr, Nd, Sm), New J. Phys. **22**, 073061 (2020).

[12] J. Finley, C. Lee, P. Y. Huang, and L. Liu, Spin–orbit torque switching in a nearly compensated Heusler ferrimagnet, Adv. Mater. **31**, 1805361 (2019).

[13] Y. You, G. Xu, F. Hu, Y. Gong, E. Liu, G. Peng, and F. Xu, Designing magnetic compensated states in tetragonal Mn_3Ge-based Heusler alloys, J. Magn. Magn. Mater. **429**, 40 (2017).

[14] A. K. Nayak *et al.*, Design of compensated ferrimagnetic Heusler alloys for giant tunable exchange bias, Nat. Mater. **14**, 679 (2015).

[15] A. Chanda, D. Rani, J. Nag, A. Alam, K. G. Suresh, M. H. Phan, and H. Srikanth, Emergence of asymmetric skew-scattering

dominated anomalous Nernst effect in the spin gapless semiconductors $Co_{1+x}Fe_{1-x}$ CrGa, Phys. Rev. B **106**, 134416 (2022).
[16] S. Ouardi, G. H. Fecher, C. Felser, and J. Kübler, Realization of spin gapless semiconductors: The Heusler compound Mn_2CoAl, Phys. Rev. Lett. **110**, 100401 (2013).
[17] G. Z. Xu, E. K. Liu, Y. Du, G. J. Li, G. D. Liu, W. H. Wang, and G. H. Wu, A new spin gapless semiconductors family: Quaternary Heusler compounds, EPL **102**, 17007 (2013).
[18] H. C. Kandpal, G. H. Fecher, and C. Felser, Calculated electronic and magnetic properties of the half-metallic, transition metal based Heusler compounds, J. Phys. D: Appl. Phys. **40**, 1507 (2007).
[19] I. Galanakis, P. Mavropoulos, and P. H. Dederichs, Electronic structure and Slater–Pauling behaviour in half-metallic Heusler alloys calculated from first principles, J. Phys. D: Appl. Phys. **39**, 765 (2006).
[20] C. Xie, H. Yuan, Z. Zhang, and X. Wang, Magnetic Weyl and quadratic nodal lines in inverse-Heusler-based fully compensated ferrimagnetic half-metals, Phys. Rev. Mater. **6**, 094406 (2022).
[21] W. Zhu, E. K. Liu, L. Feng, X. D. Tang, J. L. Chen, G. H. Wu, H. Y. Liu, F. B. Meng, and H. Z. Luo, Magnetic-field-induced transformation in femnga alloys, Appl. Phys. Lett. **95**, 222512 (2009).
[22] M. Siewert, M. E. Gruner, A. Hucht, H. C. Herper, A. Dannenberg, A. Chakrabarti, N. Singh, R. Arróyave, and P. Entel, A first-principles investigation of the compositional dependent properties of magnetic shape memory Heusler alloys, Adv. Eng. Mater. **14**, 530 (2012).
[23] T. Bachaga, J. Zhang, M. Khitouni, and J. J. Sunol, NiMn-based Heusler magnetic shape memory alloys: A review, Int. J. Adv. Manuf. Technol. **103**, 2761 (2019).
[24] T. Graf, C. Felser, and S. S. P. Parkin, Simple rules for the understanding of Heusler compounds, Prog. Solid State Chem. **39**, 1 (2011).
[25] P. Swekis *et al.*, Magnetic and electronic properties of Weyl semimetal Co_2MnGa thin films, Nanomaterials **11**, 251 (2021).
[26] S. V. Faleev, Y. Ferrante, J. Jeong, M. G. Samant, B. Jones, and S. S. P. Parkin, Origin of the tetragonal ground state of Heusler compounds, Phys. Rev. Appl. **7**, 034022 (2017).
[27] S. W. D'Souza, J. Nayak, M. Maniraj, A. Rai, R. S. Dhaka, S. R. Barman, D. L. Schlagel, T. A. Lograsso, and A. Chakrabarti, $Ni_2MnGa(100)$ ferromagnetic shape memory alloy: A surface study, Surf. Sci. **606**, 130 (2012).
[28] Z. H. Liu, M. Zhang, Y. T. Cui, Y. Q. Zhou, W. H. Wang, G. H. Wu, X. X. Zhang, and G. Xiao, Martensitic transformation and shape memory effect in ferromagnetic Heusler alloy Ni_2FeGa, Appl. Phys. Lett. **82**, 424 (2003).
[29] M. Acet, Ll. Mañosa, and A. Planes, Magnetic-field-induced effects in martensitic Heusler-based magnetic shape memory alloys, Handb. Magn. Mater. **19**, 231 (2011).
[30] M. J. Pechan, C. Yu, D. Carr, and C. J. Palmstrøm, Remarkable strain-induced magnetic anisotropy in epitaxial Co_2MnGa (001) films, J. Magn. Magn. Mater. **286**, 340 (2005).
[31] Y.-I. Matsushita, G. Madjarova, J. K. Dewhurst, S. Shallcross, C. Felser, S. Sharma, and E. K. U. Gross, Large magnetocrystalline anisotropy in tetragonally distorted Heuslers: A systematic study, J. Phys. D: Appl. Phys. **50**, 095002 (2017).
[32] V. Alijani, J. Winterlik, G. H. Fecher, and C. Felser, Tuning the magnetism of the Heusler alloys $Mn_{3-x}Co_xGa$ from soft and half-metallic to hard-magnetic for spin-transfer torque applications, Appl. Phys. Lett. **99**, 222510 (2011).
[33] T. Gasi, A. K. Nayak, J. Winterlik, V. Ksenofontov, P. Adler, M. Nicklas, and C. Felser, Exchange-spring like magnetic behavior of the tetragonal Heusler compound Mn_2FeGa as a candidate for spin-transfer torque, Appl. Phys. Lett. **102**, 202402 (2013).
[34] J. Winterlik *et al.*, Design scheme of new tetragonal Heusler compounds for spin-transfer torque applications and its experimental realization, Adv. Mater. **24**, 6283 (2012).
[35] K. Manna *et al.*, From colossal to zero: Controlling the anomalous Hall effect in magnetic Heusler compounds via berry curvature design, Phys. Rev. X **8**, 041045 (2018).
[36] G. Chang *et al.*, Topological Hopf and chain link semimetal states and their application to Co_2MnGa, Phys. Rev. Lett. **119**, 156401 (2017).
[37] G. Chang *et al.*, Room-temperature magnetic topological Weyl fermion and nodal line semimetal states in half-metallic Heusler Co_2TiX (X = Si, Ge, or Sn), Sci. Rep. **6**, 38839 (2016).
[38] M. Lucht, M. Lerche, H.-C. Wille, Yu. V. Shvyd'ko, H. D. Rüter, E. Gerdau, and P. Becker, Precise measurement of the lattice parameters of α-Al_2O_3 in the temperature range 4.5–250 K using the Mössbauer wavelength standard, J. Appl. Crystallogr. **36**, 1075 (2003).
[39] See Supplemental Material at http://link.aps.org/supplemental/10.1103/PhysRevB.110.054419 for further information regarding the normalized temperature dependence of c for the substrate and film; the reciprocal space mapping of the (220) x-ray diffraction peak; the full list of calculated band structures for different c/a ratios; a schematic representation of the Weyl distances; the high-field magnetization versus temperature data, and its kinetic arrest of the tetragonal distortion; further MFM scans at different temperatures and scales; the autocorrelation and phase distribution spectra used for extracting the domain width and rms phase deviation; the temperature-dependent magnetoresistance of the film; and the exchange stiffness fitting.
[40] A. Markou *et al.*, Thickness dependence of the anomalous Hall effect in thin films of the topological semimetal Co_2MnGa, Phys. Rev. B **100**, 054422 (2019).
[41] A. Banerjee, P. Chaddah, S. Dash, K. Kumar, A. Lakhani, X. Chen, and R. V. Ramanujan, History-dependent nucleation and growth of the martensitic phase in the magnetic shape memory alloy $Ni_{45}Co_5Mn_{38}Sn_{12}$, Phys. Rev. B **84**, 214420 (2011).
[42] R. Y. Umetsu, K. Ito, W. Ito, K. Koyama, T. Kanomata, K. Ishida, and R. Kainuma, Kinetic arrest behavior in martensitic transformation of NiCoMnSn metamagnetic shape memory alloy, J. Alloys Compd. **509**, 1389 (2011).
[43] P. J. Brown, A. Y. Bargawi, J. Crangle, K.-U. Neumann, and K. R. A. Ziebeck, Direct observation of a band Jahn-Teller effect in the martensitic phase transition of Ni_2MnGa, J. Phys.: Condens. Matter **11**, 4715 (1999).
[44] C. Hao, Y. Wang, J. Wang, C. Liang, D. Duan, D. Wang, S. Yang, and X. Song, Kinetic arrest behavior in Ni-Co-Mn-Sn alloys within the phase boundary between martensite and strain glass, Scr. Mater. **194**, 113671 (2021).
[45] A. Chanda, J. E. Shoup, N. Schulz, D. A. Arena, and H. Srikanth, Tunable competing magnetic anisotropies and spin reconfigurations in ferrimagnetic $Fe_{100-x}Gd_x$ Alloy Films, Phys. Rev. B **104**, 094404 (2021).

[46] N. Schulz, A. Chanda, G. Datt, M. V. Kamalakar, T. Sarkar, M. H. Phan, and H. Srikanth, Proximity enhanced magnetism at $NiFe_2O_4$/graphene interface, AIP Adv. **12**, 035132 (2022).

[47] H. Srikanth and S. Chandra, *Magnetic Measurement Techniques for Materials Characterization* (Springer, Berlin, 2021).

[48] H. Srikanth, J. Wiggins, and H. Rees, Radio-frequency impedance measurements using a tunnel-diode oscillator technique, Rev. Sci. Instrum. **70**, 3097 (1999).

[49] N. Schulz *et al.*, Surface termination-enhanced magnetism at nickel ferrite/2D nanomaterial interfaces: Implications for spintronics, ACS Appl. Nano Mater. **6**, 10402 (2023).

[50] N. A. Frey Huls, N. S. Bingham, M. H. Phan, H. Srikanth, D. D. Stauffer, and C. Leighton, Transverse susceptibility as a probe of the magnetocrystalline anisotropy-driven phase transition in $Pr_{0.5}Sr_{0.5}CoO_3$, Phys. Rev. B **83**, 024406 (2011).

[51] S. Lepadatu, G. Mckenzie, T. Mercer, C. R. MacKinnon, and P. R. Bissell, Computation of magnetization, exchange stiffness, anisotropy, and susceptibilities in large-scale systems using GPU-accelerated atomistic parallel Monte Carlo algorithms, J. Magn. Magn. Mater. **540**, 168460 (2021).

[52] S. J. Yun *et al.*, Escalating ferromagnetic order via se-vacancies near vanadium in WSe_2 monolayers, Adv. Mater. **34**, 2106551 (2022).

[53] M. Bramowicz, S. Kulesza, P. Czaja, and W. Maziarz, Application of the autocorrelation function and fractal geometry methods for analysis of MFM images, Arch. Metall. Mater. **59**, 451 (2014).

[54] A. Yamada and Y. Fuseya, Negative magnetoresistance and sign change of the planar Hall effect due to negative off-diagonal effective mass in Weyl semimetals, Phys. Rev. B **105**, 205207 (2022).

[55] Y. Li, Z. Wang, P. Li, X. Yang, Z. Shen, F. Sheng, X. Li, Y. Lu, Y. Zheng, and Z.-A. Xu, Negative magnetoresistance in Weyl semimetals NbAs and NbP: Intrinsic chiral anomaly and extrinsic effects, Front. Phys. **12**, 127205 (2017).

[56] F. Arnold *et al.*, Negative magnetoresistance without well-defined chirality in the Weyl semimetal TaP, Nat. Commun. **7**, 11615 (2016).

[57] D. Wortmann *et al.*, FLEUR (MaX-R7.1), Zenodo (2024), https://doi.org/10.5281/zenodo.10844167.

[58] J. P. Perdew, K. Burke, and M. Ernzerhof, Generalized gradient approximation made simple, Phys. Rev. Lett. **77**, 3865 (1996).

[59] J. M. Perez-Mato, S. V. Gallego, E. S. Tasci, L. Elcoro, G. de la Flor, and M. I. Aroyo, Symmetry-based computational tools for magnetic crystallography, Annu. Rev. Mater. Res. **45**, 217 (2015).

[60] H. T. Stokes and D. M. Hatch, FINDSYM: Program for identifying the space-group symmetry of a crystal, J. Appl. Crystallogr. **38**, 237 (2005).